Solar Energy Materials & Solar Cells 278 (2024) 113188

Contents lists available at ScienceDirect

Solar Energy Materials and Solar Cells

journal homepage: www.elsevier.com/locate/solmat

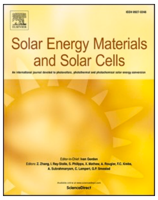

Unveiling the origin of metal contact failures in TOPCon solar cells through accelerated damp-heat testing

Xinyuan Wu [a,*], Chandany Sen [a], Xutao Wang [a], Yuhao Cheng [a], Ruirui Lv [b], Hao Song [b], Yuanjie Yu [b], Baochen Liao [c], Sheng Ma [d], Muhammad Umair Khan [a], Alison Ciesla [a], Bram Hoex [a,**]

[a] *School of Photovoltaic and Renewable Energy Engineering, University of New South Wales, Sydney, 2052, Australia*
[b] *Canadian Solar Inc., Suzhou, Jiangsu, 215129, China*
[c] *School of Microelectronics and School of Integrated Circuits, Nantong University, Nantong, Jiangsu, 226019, China*
[d] *Institute of Solar Energy, Shanghai Jiao Tong University, Shanghai, 200240, China*

ARTICLE INFO

Keywords:
Photovoltaics
Tunnel oxide passivated contact (TOPCon)
Damp-heat stability
Silicon solar cells
Metallisation reliability
Corrosion
Na-related salts

ABSTRACT

Tunnel oxide passivated contact (TOPCon) solar cells are expected to dominate the global photovoltaic market in the coming decade thanks to rapid advancements in power conversion efficiency (*PCE*). However, there are concerns about the reliability of TOPCon modules, particularly in hot and humid conditions. The current module-level fundamental analysis strategies for TOPCon solar cells provide too slow feedback for rapid process development. This study explores the degradation of metal contacts in TOPCon solar cells under accelerated testing conditions of 85 °C and 85 % relative humidity (DH85). The degradation was induced by two commonly used sodium-related salts, sodium bicarbonate ($NaHCO_3$) and sodium chloride (NaCl), in the testing of the solar cells. When applied to the front side, $NaHCO_3$ caused a $\sim 5\%_{rel}$ *PCE* reduction after 100-h DH85 exposure, while NaCl leads to a more significant $\sim 92\%_{rel}$ *PCE* reduction. The primary cause of degradation is a considerable increase in series resistance (R_s), likely due to electrochemical reactions within the Ag/Al paste. When the salts are applied to the rear of the TOPCon solar cell, the degradation becomes more complex. $NaHCO_3$ increases recombination and results in a deterioration of the contact, resulting in a $\sim 16\%_{rel}$ *PCE* reduction after 100-h DH85 testing. Conversely, NaCl primarily causes a decline in open-circuit voltage (V_{oc}) and a $\sim 4\%_{rel}$ *PCE* loss. This manuscript primarily investigates degradation mechanisms related on the rear side, with a focus on significant oxidation occurring at the interface between Ag and Si. These findings highlight the susceptibility of TOPCon solar cells to contact corrosion, emphasizing the electrochemical reactivity of metallisation as a potential risk for long-term TOPCon module operation. This study provides crucial insights into TOPCon cell degradation mechanisms, which are essential for optimising performance and enhancing the long-term reliability of TOPCon modules.

1. Introduction

Tunnel oxide passivated contact (TOPCon) solar cells have emerged as a promising strategy to reach the limiting efficiency of single junction silicon solar cells in industrial production. The seminal work by Feldman et al., in 2013 introduced the TOPCon structure, showcasing a noteworthy 23.0 % champion efficiency [1,2]. Subsequently, extensive research efforts by numerous scientists and engineers have propelled the evolution of TOPCon solar cells, leveraging optimised technique routes and advanced equipment [3–13]. This concerted effort has ushered in a new era for TOPCon solar cells, with the best reported company efficiency of 25.6 % on M10 silicon wafers by JA Solar [14]. The cost-effectiveness and impressive performance metrics of TOPCon solar cells have garnered substantial industry attention. Forecasts from the ITRPV 2024 report suggest that TOPCon solar cells have superseded passivated emitter and rear contact (PERC) technology [15]. As expected, alongside enhancements in cell efficiency, TOPCon module performance has made impressive progress, surpassing that of PERC

---

* Corresponding author.
** Corresponding author.
E-mail addresses: xinyuan.wu@unsw.edu.au (X. Wu), b.hoex@unsw.edu.au (B. Hoex).

https://doi.org/10.1016/j.solmat.2024.113188
Received 22 August 2024; Received in revised form 8 September 2024; Accepted 23 September 2024

modules. For instance, Astronergy has demonstrated a module efficiency of 22.8 % with a glass-glass design, surpassing the best PERC module efficiency of 21.7 % [16].

However, while the remarkable performance improvements underscore the potential of TOPCon technology, concerns loom over module reliability, a critical aspect of its commercial viability. Peters et al. emphasised that lower degradation rates contribute to extended system lifetimes, possibly reaching up to 50 years [17]. Yet, there are indications from researchers that TOPCon solar cells may encounter failure risks under prolonged operational (or testing) conditions, notably exhibiting significant degradation under damp-heat conditions (DH85, 85 °C, 85 % relative humidity) [18,19]. This degradation, attributed to factors like moisture, high temperature, acetic acid exposure, and sodium-related contamination, raises concerns about the stability of TOPCon modules during extended operation [18–20].

The lifetime of solar modules involves the gradual diffusion of ions into cells' surfaces and bulk, facilitated by moisture or a potential difference between the cell and the module frame [21,22]. This process can trigger electrochemical reactions and corrosion. For instance, Segbefia et al. noted that moisture played a significant role in the formation of various by-products on the cells' surfaces of 20-year-old, field-aged solar cell modules. These included titania metal complexes from anti-reflective coatings, phosphate compounds from encapsulant materials, sodium residues from the glass, carbonates and acetates from encapsulant materials, and other metal ions from solar cell metallisation and soldering ribbons [23]. Under conditions like damp-heat, the presence of sodium ions accelerates chemical corrosion reactions, causing swift degradation [20,24–28]. The process could involve sodium ions (Na^+) associating with a diverse array of anions, which may originate from the bill of module materials or be introduced as contaminants from the environment. HCO_3^- may originate from the glass and, along with Na^+, can degrade solar cells under damp-heat conditions. Some researchers have used $NaHCO_3$ solution as an external contaminant to accelerate and study the degradation of solar cells in these conditions [25,26,29]. Chloride (Cl^-) has been detected in field-aged modules, likely originating from the natural water cycle [23,30–32]. Cl^- can be introduced by environmental factors such as rainwater, soil, dust, and seawater, which may infiltrate and come into direct contact with solar cells [20,30–32]. Consequently, to simulate and accelerate degradation in damp-heat testing, some studies have used NaCl combined with Na^+ [20,24,33]. Each of these interactions triggers distinct chemical reactions, which, in turn, differentially affect the components within the cell [23,34–37].

Despite the advancements in TOPCon technology, the reliability and specific degradation mechanisms under DH85 conditions remain inadequately explored compared with the PERC technique. Therefore, a comprehensive understanding of how diverse ions affect TOPCon solar cells and contribute to degradation is imperative. In this study, we go into the degradation of TOPCon solar cells caused by various Na salts under damp-heat conditions. Through detailed analysis of elemental distribution, we unveil cell-level metal contact failure mechanisms induced by these contaminants. Furthermore, we propose several degradation models to elucidate and differentiate failures stemming from contacts, providing crucial insights into the reliability of TOPCon technology.

2. Experimental details

All experiments used G1 n-type TOPCon solar cells with 5 busbars (158.75 mm × 158.75 mm). As shown in Fig. 1, the cells' pyramid-textured front side featured a boron-diffused emitter covered with aluminium oxide (Al_2O_3) and silicon nitride (SiN_x), silicon oxynitride (SiO_yN_z) stack providing surface passivation and serving as antireflection coating (ARC). On the rear side, the solar cell featured a tunnelling silicon oxide (SiO_2) layer paired with a phosphorus-doped poly-Si layer, forming the n-type TOPCon structure, capped with a SiN_x layer ARC. The front-side metallisation comprised a combination of silver (Ag) and aluminium (Al, 3–5 at.%) as the conducting material, while the rear-side metal contact solely consists of Ag for conduction.

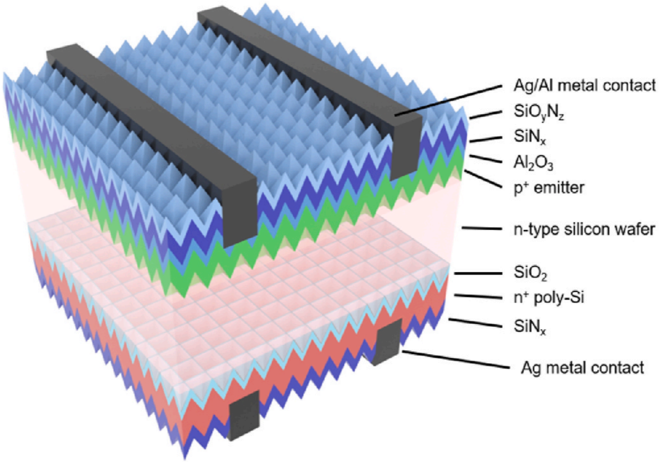

Fig. 1. Schematic of TOPCon solar cells used in this work.

The experiment flow is shown as Fig. 2. Before the experiments, all the solar cells were cleaned by deionised water (DIW) and fast-dried with a nitrogen gun to ensure that the solar cells were clear prior to the experiments. Sodium bicarbonate ($NaHCO_3$) and sodium chloride (NaCl) were used as the Na-containing contaminants for the accelerated DH85 test. Samples were divided into 5 groups (at least 4 cells for each experiment group): Group 1 refers to the control samples only treated with DIW; Group 2 and 3 refer to samples exposed to $NaHCO_3$ at the front ($NaHCO_3$-front) or rear ($NaHCO_3$-rear) side; Group 4 and 5 refer to samples exposed to NaCl at the front (NaCl-front) or rear (NaCl-rear) sides. Around 0.3g solution was sprayed on the sample surface for each sample, and the samples were naturally dried in the fume cupboard at room temperature and atmosphere. Each salt had a Na concentration of 0.155 mol/L. We took care to avoid potential contamination within and between samples. Subsequently, samples were placed vertically in polytetrafluoroethylene (PTFE) cassettes and isolated from each other to avoid cross-contamination during the damp-heat testing. An ASLi Environment chamber at $T = 85$ °C and a relative humidity of 85 % was used for the damp heat testing (DH85). Before each measurement, the climate chamber was cooled down to room temperature and heated up again for the next stage of damp-heat treatment.

We utilised a LOANA solar cell analysis system from pv-tools equipped with a 5-rail pin contact frame to examine the current-voltage (*I-V*) characteristics of solar cells. The series resistance (R_s) values were measured using the multi-light method (MLM) at illumination levels of 0.9, 1.0, and 1.1 suns. Calibration of the system's alignment and measurement stability was achieved using multiple reference cells, ensuring consistent measurement of the short-circuit current density (J_{sc}) and fill factor (*FF*) throughout the entire DH85 test. A BTimaging R3 tool with a high open-circuit voltage lens was used to generate photoluminescence (PL) and series resistance images. All luminescence images were taken at the front sides of the TOPCon solar cells. We used LumiTools for luminescence image processing, and the exposure time was chosen so that the PL intensity was not saturated (<50,000 counts) and a 0 to 4 Ohmcm^2 range was used for the R_s images [38]. To measure contact resistivity, we selected the non-busbar regions of the TOPCon cells and used a FOBA M1000 scribing laser to cut them into 6 mm wide stripes. The contact resistivity (ρ_c) of the front and rear sides were measured using the transfer length method (TLM) using a pv-tools TLM-SCAN$^+$.

Furthermore, scanning electron microscopy (SEM) images were obtained to study the metal contact and cells' surface. Top-view SEM images were captured by FEI Nova NanoSEM 450 FE-SEM at 10 kV

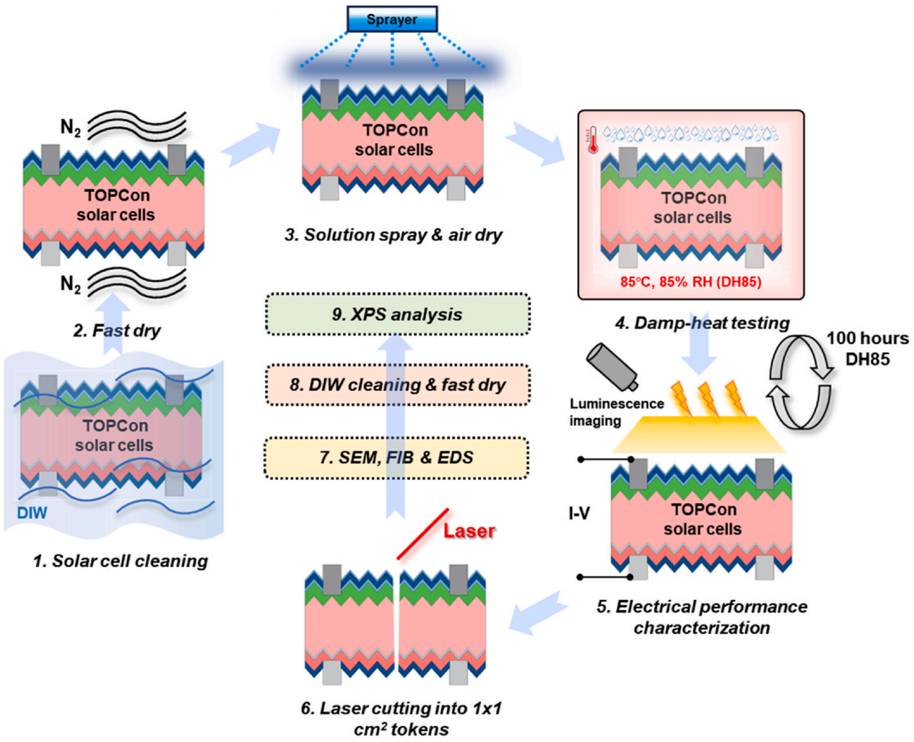

Fig. 2. Experimental flow chart used in this work.

operating voltage. Under the same SEM conditions, energy dispersive spectroscopy (EDS) analysis was conducted by the Oxford Instruments Ultim® Max, and the results were processed with AZtec software to track and analyse the element information. In addition, we employed Zeiss 550 Crossbeam cryo-focused ion-beam scanning electron microscope (cryo-FIB-SEM) for cross-section images of metal contact analysis. The stage was tilted 54° and vertically to the FIB gun during the FIB session. The SEM images were obtained at 36° to the sample surfaces, and the images and scales were adjusted based on this tilt angle. The SEM probe current was 1.5 nA, and the electron high tension (EHT) voltage was 20 kV. The FIB probe was set up to 30 kV and 50 pA under standard kV mode. We also applied the same type of EDS tool to analyse the element information on the cross-section images. For X-ray photoelectron spectroscopy (XPS) analysis, the samples were cleaned by DIW and conducted by Thermo ESCALAB250Xi X-ray photoelectron spectrometer. The XPS system utilised a monochromatic Al K alpha X-ray source with an energy of 1486.68 eV and a power of 120 W. The reference binding energy was set at 284.8 eV for the C1s peak to account for adventitious hydrocarbon.

3. Results and discussion

3.1. Cell-level measurements

The initial performance of the 30 cells was measured, and the corresponding results, including standard deviations, are summarised in Table 1. The average measured power conversion efficiency (*PCE)* of the cells was around 23.1 %. The standard deviations were found to be small for all parameters, thus indicating that all solar cells were comparable, which is to be expected for industrial solar cells.

Table 1
The average testing TOPCon cell performance before DH85 testing.

Number of cells	*PCE* (%)	J_{sc} (mA/cm^2)	V_{oc} (mV)	*FF* (%)	Multiple light R_s (Ohmcm^2)
30	23.1 ± 0.1	40.1 ± 0.1	700.5 ± 0.8	82.4 ± 0.5	0.37 ± 0.06

The Group 1 samples were found to be relatively stable after 100 h of DH85. As shown in Fig. 3 and Table 2, the efficiency only decreased by 0.44 %, mainly driven by a 0.55 % drop in *FF*. These results indicate that exposing TOPCon cells to high humidity at elevated temperatures for extended periods did not inherently lead to degradation.

However, cells exposed to Na-salts were not stable. As shown in Table 2, $NaHCO_3$-exposed cells (both front and rear) showed a notable reduction in *PCE*, with relative decreases of ~5.2 % and ~16.0 %, respectively, after 100 h of DH85. The degradation of the $NaHCO_3$-front cells was primarily attributed to a significant increase in R_s (~210 % relative increase). Meanwhile, the $NaHCO_3$-rear cells experienced not only a substantial increase in R_s (~450%$_{rel}$ increase) but also a significant reduction in V_{oc} (~4.3 % relative decrease) after 100 h of DH85. Notably, the V_{oc} drop of the $NaHCO_3$-rear cells occurred within the first 20 h and remained stable thereafter, while the increase in R_s was not prominently observed until after 10 h of testing, continuing to rise until the conclusion of the experiment. Consequently, the *PCE* of $NaHCO_3$-rear cells decreased rapidly within the initial 20 h due to the combined effect of V_{oc} reduction and an increase R_s.

During the entire testing duration, NaCl-front cells exhibited the most severe increase in R_s up to ~10,000 %. Additionally, a significant decrease in J_{sc} was observed after 6 h, most likely resulting from a poor current extraction. A slight decrease in V_{oc} (~0.89%$_{rel}$) was also noted. NaCl-rear cells experienced a relative *PCE* degradation of ~3.7 %, primarily attributed to a V_{oc} loss (~1.8 % relative decrease), while other parameters such as J_{sc} (~0.47 % relative decrease) and R_s (~13 % relative increase) remained relatively stable after 100 h of DH 85.

Fig. 4 shows the PL images captured at various stages of the DH85 test, while Table 3 illustrates the count variations. During the damp-heat testing, the repeatability of PL and R_s imaging was verified by a reference sample, avoiding systematic errors. All samples were positioned at the same location on the testing stage to allow for direct comparison. It is evident that the control group remained stable (~1.6%$_{rel}$) throughout the DH85 period, affirming the adequacy of our pre-cleaning procedure and suggesting that the damp-heat test alone did not lead to sample

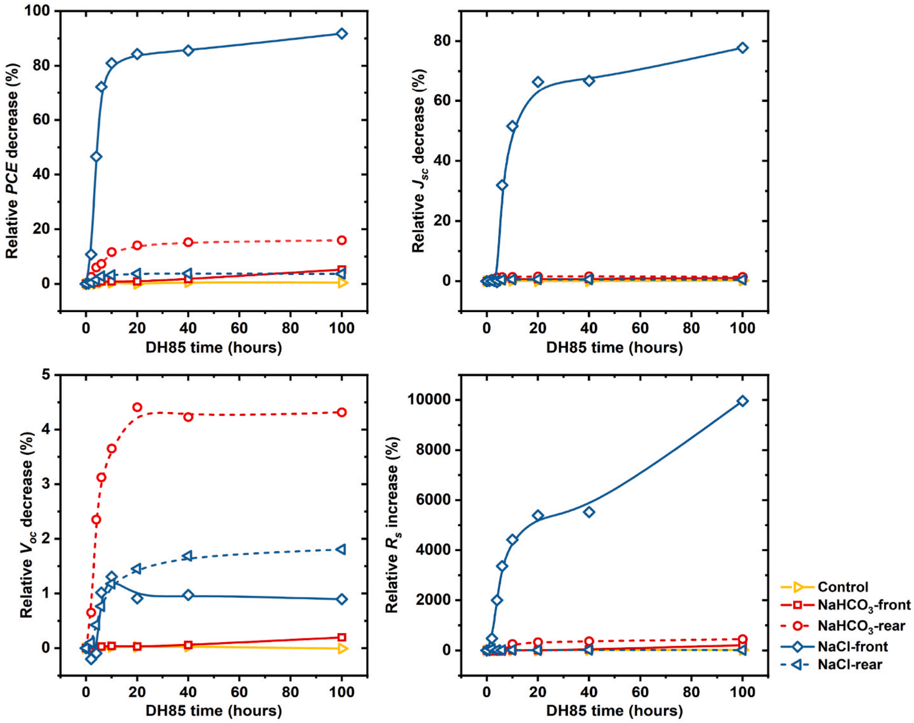

Fig. 3. Relative changes in *PCE*, J_{sc}, V_{oc}, *FF* and R_s as a function of DH85 duration for the experimental groups.

Table 2
Summary of the relative one-*Sun*I-V parameters of TOPCon solar cells after the 100-h DH85 test.

Parameter variation	Control	NaHCO$_3$		NaCl	
		front	rear	front	rear
PCE	−0.44 %	−5.2 %	−16 %	−92 %	−3.7 %
J_{sc}	−0.22 %	−1.1 %	−1.4 %	−78 %	−0.47 %
V_{oc}	0.01 %	−0.2 %	−4.3 %	−0.89 %	−1.8 %
FF	−0.55 %	−4.0 %	−11 %	−63 %	−1.6 %
R_s	21 %	210 %	450 %	10,000 %	13 %

degradation. The PL counts of the NaHCO$_3$-front were found to be relatively stable, with only a decrease of ~5.0%$_{rel}$ observed after 100 h of DH85, mainly attributed to faint recombination traces along the busbars. Conversely, the NaHCO$_3$-rear sample displayed a noticeable reduction in the overall PL intensity, experiencing a more substantial relative drop of ~68 % during the 100-h DH85 test. This decline was apparent from the initial stages of DH85 testing, with evidence of degradation observed both in the coating and metallisation regions, as indicated by the close up of the PL images.

In the case of NaCl-front, there was a reduction of ~4.7%$_{rel}$ in PL counts after 100 h, with degradation primarily localised adjacent to the metallisation regions. Furthermore, a uniform decrease in PL counts was observed for NaCl-rear samples, with a relative value of ~34 %, which was less pronounced compared to the NaHCO$_3$-rear sample. Nevertheless, similar to NaHCO$_3$-rear, we can see an uniform decrease in the PL images (which were taken from the front sides of the cells) for the cell exposed to NaCl at the rear, as shown in Fig. 4. This suggests that NaCl exposure results in a significant and uniform increase in recombination on the rear side of the TOPCon solar cell during DH85, which is consistent with the 1.8 % reduction in V_{oc}, as shown in Table 2.

Fig. 5 illustrates the R_s images after various DH85 times, revealing distinct trends among different treatment groups. The control group exhibited a negligible R_s increase over the entire testing period, with a relative increase of ~20 %. The NaHCO$_3$-front sample showed a substantial relative increase in average R_s of ~320 %, particularly accentuated in certain regions, notably at the periphery, following 100 h of DH85. Meanwhile, NaHCO$_3$-rear exhibited a remarkable ~860%$_{rel}$ increase in R_s count. Unlike the front side, the rear side exhibited pronounced localised increases in R_s, predominantly in the central regions of the solar cell. Furthermore, NaCl-front exhibited a dramatic ~2800 % increase in average R_s throughout the testing period, with immediate and non-localised R_s increase already evident after 4 h of DH85. Unfortunately, after 100 h of DH85, certain regions experienced R_s increases beyond the validity of the measurement technique [39]. In contrast, the NaCl-rear sample displayed a minimal ~14%$_{rel}$ increase in average R_s after 100 h of DH85, akin to the control group.

These findings are consistent with the previously discussed *I-V* results illustrated in Fig. 3 and summarised in Table 2. Treatment with NaHCO$_3$ led to a decrease in R_s on both the front and rear sides of TOPCon solar cells, with the primary V_{oc} reduction observed when NaHCO$_3$ solution was applied to the rear side. In contrast, NaCl treatment resulted in a rapid and severe increase in R_s, accompanied by a slight rise in recombination on the front side, while resulting in an increase in recombination at the rear side, thereby lowering the V_{oc}, without displaying any R_s issues. This indicates that Na$^+$ may degrade the solar cells in different ways depending on the accompanying anions, likely due to differences in their chemical properties.

3.2. Resistance measurements

To investigate the contact degradation further, TLM measurements were used to extract ρ_c for the screen-printed contacts. Fig. 6 depicts variations in ρ_c for both the front and rear sides of TOPCon solar cells. The initial measurements were taken before exposure to the salt solutions. Following a 40-h DH85 test, all front-side samples showed varying degrees of R_s degradation, with average ρ_c increasing from approximately 1.0 to 1.6 mΩ cm^2 for the Control-front group, from 1.6 to 4.1 mΩ cm^2 for the NaHCO$_3$-front group, and from 1.0 to 490 mΩ cm^2 for the NaCl-front group. The ρ_c of the NaCl-front group exhibited a dramatic rise, consistent with *I-V* results and R_s images, while NaHCO$_3$-front showed a slower and less pronounced R_s decrease during testing. Among the rear-side groups, only NaHCO$_3$-rear showed an increase in

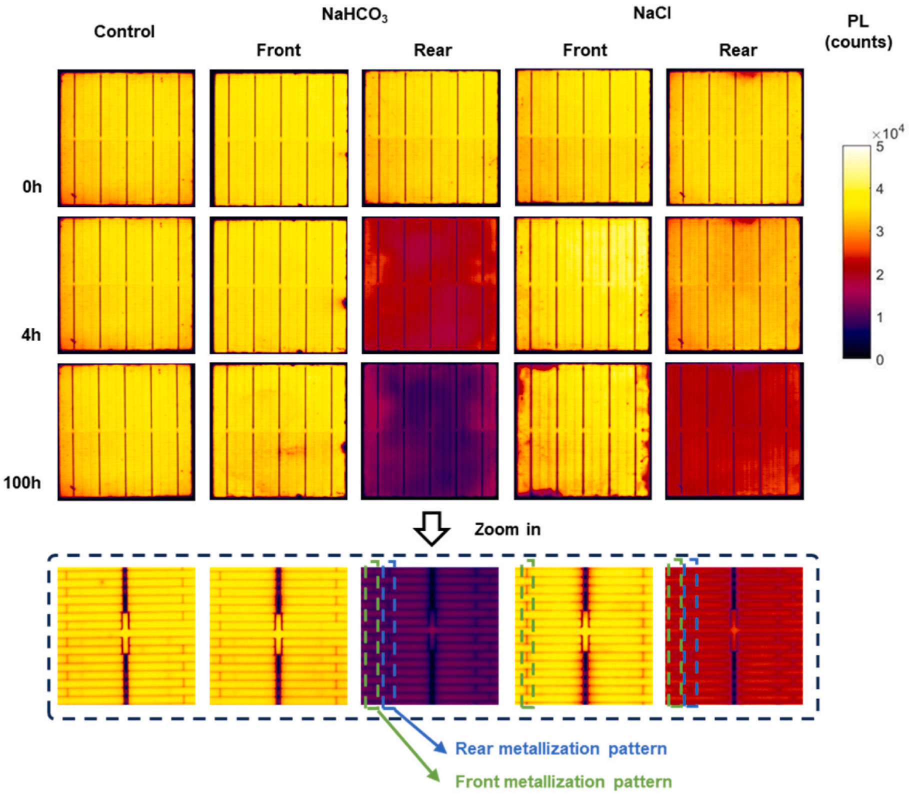

Fig. 4. PL images of TOPCon cells from each experimental group taken at various stages (0, 4 and 100 h) during DH85 test.

Table 3
The change in the average luminescence intensity and average R_s of TOPCon solar cells after a 100-h DH85 test.

Group	PL intensity change	Average R_s change
Control	1.6 %	20 %
$NaHCO_3$-front	−5.0 %	320 %
$NaHCO_3$-rear	−68 %	860 %
NaCl-front	−4.7 %	2800 %
NaCl-rear	−34 %	14 %

ρ_c, rising from approximately 0.7 to 2.1 mΩ cm^2, while NaCl-rear and Control-rear groups showed no obvious ρ_c change during DH85 testing, maintaining values around 0.6 mΩ cm^2. The rear side appeared more stable than the front side, likely due to differences in paste composition, particle size, and pattern design.

The line resistances of experimental samples were also measured, and the results are shown in Fig. 7. The Control-front and Control-rear groups had line resistivities of approximately 0.94 Ω/cm and 0.93 Ω/cm, respectively. $NaHCO_3$-front showed a slight increase in line resistance to approximately 1.1 Ω/cm, while NaCl-front had a value of roughly 1.5 Ω/cm. Rear-side values remained similar, with values of 0.91 Ω/cm for $NaHCO_3$-rear and 0.83 Ω/cm for NaCl-rear, respectively.

As depicted in Fig. 8, a front-side series resistance loss analysis was

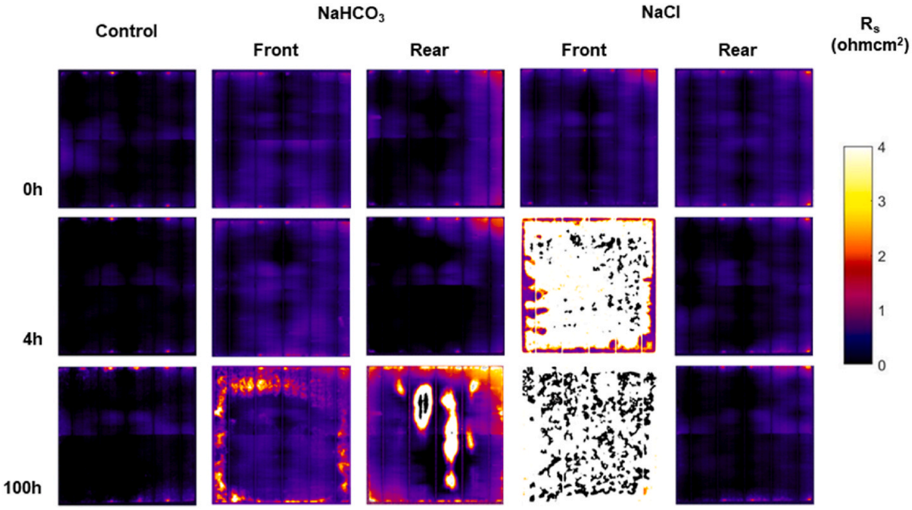

Fig. 5. R_s images of TOPCon cells from each experimental group taken at various stages (0, 4 and 100 h) of the DH85 test.

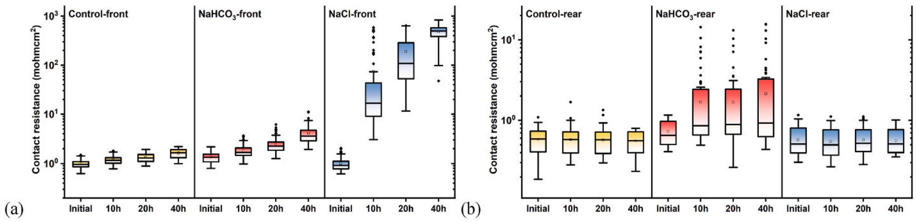

Fig. 6. Contact resistivities (ρ_c) of the (a) front sides and (b) rear sides after various DH85 durations for the control, NaHCO$_3$ and NaCl samples.

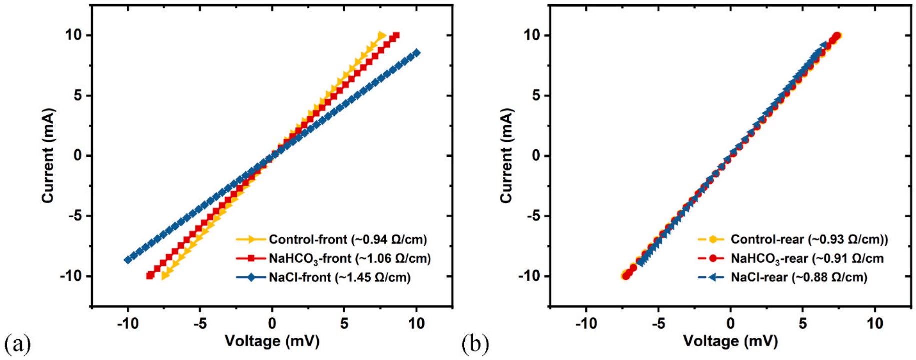

Fig. 7. *I-V* measurement on the (a) front-side and (b) rear-side metal finger for the control, NaHCO$_3$ and NaCl samples after 100 h of DH85. The value for the line resistance extracted from the slope of the *I-V* measurement is indicated in the graph as well.

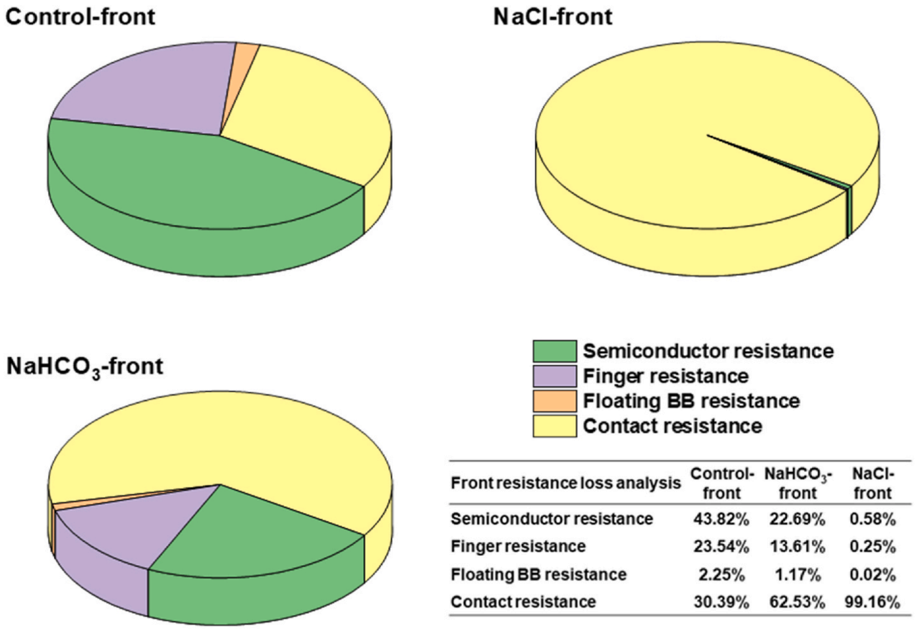

Front resistance loss analysis	Control-front	NaHCO$_3$-front	NaCl-front
Semiconductor resistance	43.82%	22.69%	0.58%
Finger resistance	23.54%	13.61%	0.25%
Floating BB resistance	2.25%	1.17%	0.02%
Contact resistance	30.39%	62.53%	99.16%

Fig. 8. Analysis of front resistance loss in front-exposed groups using Griddler 2.5 PRO [40].

conducted using Griddler 2.5 PRO [40]. The primary input changes were the contact resistivity and line resistance extracted from Figs. 6 and 7. For the NaCl-front, the main contributor to the series resistance loss was the increase in contact resistivity (~99 % of the additional front resistance loss). In the simulation for the NaHCO$_3$-front, the contact resistivity was also found to be the primary factor (~62 % of the additional front resistance loss) contributing to the series resistance. Based on these simulations, the increase in series resistance was primarily due to the rise in contact resistivity.

Based on previous measured and simulated results, it is evident that both NaHCO$_3$ and NaCl degrade the front contact in terms of resistance. However, the increase in front resistance is more pronounced with NaCl, indicating that NaCl is more reactive and aggressive in causing front metal/Si interface and line resistance failures compared to NaHCO$_3$. For the rear-side groups, the line resistance remained unchanged, but only the NaHCO$_3$-rear sample showed increased contact resistivity. This suggests that rear-side degradation in the NaHCO$_3$-rear sample is solely due to failures at the metal/Si interface. NaCl did not affect the rear side contact, indicating that NaCl is unlikely to degrade the Al-free Ag paste which is consistent with our previous work [33].

3.3. SEM images

Top-view SEM imaging and EDS analysis were employed to investigate surface and contact anomalies. Fig. 9 illustrates surface analysis depicting the distribution of contact elements such as Ag, Si, O, and Na on both front and rear contacts after undergoing 100 h of DH85. The analysis depth was approximately 1~2 μm based on the EDS settings used in this work. This examination revealed a significant deviation in particle size and structure from TOPCon metallisation compared to our earlier findings on silicon heterojunction (SHJ) solar cells [20,24]. Despite contact degradation in this study, TOPCon front contacts showed no notable changes in the Ag metallisation based on SEM images [20,24]. In standard TOPCon processes, high-temperature firing causes lead silicate glass to melt and dissolve Ag particles, which then fluidize and etch the silicon nitride layer. Upon cooling, Ag and lead separate, with Ag crystallizing at the Si surface. This process enhances the bonding between individual Ag particles, creating a more cohesive and robust network. The stronger interconnections between the particles reduce the likelihood of structural failure or separation, ensuring the overall Ag structure remains intact. Therefore, the preservation of Ag structures after DH85 testing can be attributed to the reinforcement and enhanced interconnections of Ag particles [41–44].

In Fig. 9 (a), Control-front SEM images and EDS analysis exhibit clear element distribution and boundaries between metal and non-metal regions with no significant Na signal. However, in $NaHCO_3$- font samples, isolated instances of Na and O were observed exclusively on the metal contact areas. Conversely, the NaCl-front sample, which had the largest increase in R_s, displayed substantial Na presence, notably within the ARC region rather than on the metal itself. This suggests that most Na applied on the screen-printed metal had likely penetrated the metal contacts and could no longer be detected by EDS.

Control-rear samples also demonstrate similar Ag, Si, and O distribution as the Control-front samples, with no Na signal detected. Analysis of rear contacts in Fig. 9 (b) shows that $NaHCO_3$-treated samples, which exhibited significant R_s increases, also present the highest Na concentrations, particularly between the ARC and metal regions, with increased intensity near metal contacts, accompanied by a decrease in detected silicon intensity. Na and O sporadically co-existed on the metal surface. Na signals from NaCl-rear samples were scattered along metal fingers distributed on the ARC surface.

When comparing the Na signal distribution across the experimental groups, Na salts exhibit different behaviour on front and rear surfaces. Ag structures remained robust across groups, except for $NaHCO_3$-rear, with no significant change in key element distribution, such as O and Si, in other groups. The presence of $NaHCO_3$ may lead to the formation of additional oxides on the cell surfaces. However, detecting degradation within the metal contacts is limited with top-view SEM images and surface EDS analysis. Therefore, cross-sectional SEM images are essential for further identifying the cause of degradation.

A combination of FIB and EDS techniques was employed to examine the metal contact properties of samples after 100 h of DH85, as illustrated in Figs. 10 and 11. In the Control-front group, the metallisation fingers exhibited close integration, facilitated by the presence of glass frit components such as lead oxide (PbO). In the realm of industrial TOPCon solar cells, the prevalent use of Al/Ag paste for front-side metallisation aims to minimise the contact resistivity between the metal and the boron-doped emitter [45–47]. SEM and EDS analyses distinctly revealed the presence of Ag and Al particles in the Control-front group, as illustrated in Fig. 10 (a). Particularly noteworthy was the observation of Al predominantly as clusters within the Ag matrix, consistent with findings from prior studies [45–47]. Moreover, no Na and Cl were detected in the Control-front samples.

In contrast to the control-front samples, those exposed to $NaHCO_3$ and NaCl exhibited areas resembling corrosion-like structures, as shown in Fig. 10 (a). EDS mappings highlighted dispersed Al and O signals in the contaminated groups rather than localised clustering, with significant O signal distributions accompanying the Al signal areas, indicating corrosion of Al clusters in metal contacts. This could contribute to the increase in line resistance. as shown in Fig. 7. Furthermore, in NaCl-front samples from Fig. 10 (a), noticeable Cl residues were primarily found in Al-associated voids or Pb regions within the metal contacts. The inconsistent correlation between Na and Cl signals raised concerns about the infiltration of Na^+ into the metal/Si surface, potentially increasing recombination. Considering Cl ions' propensity to bind with metal elements like Pb and Al, this could deteriorate the contact between silicon and the screen-printed contact [48–51].

To explore the contact interface in more detail, SEM images at higher magnification were captured and presented in Fig. 10 (b). In the Control-front samples, the interface glass layer exhibited uniform bonding between the metal and Si. Additionally, the Al signal was mixed with Pb and highly localised at a specific interface region between Ag and Si, potentially indicating the presence of Ag/Al spikes on the silicon

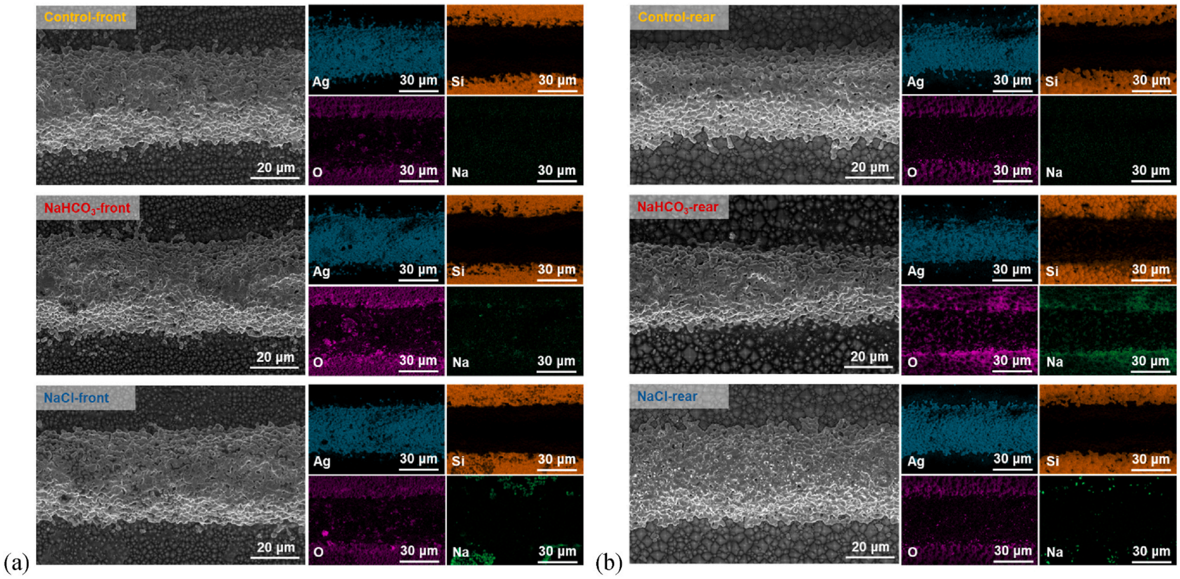

Fig. 9. Top-view SEM images and EDS analysis of (a) front and (b) rear metal contacts for the control, $NaHCO_3$, and NaCl samples after 100-h DH85. Please note that the samples were not cleaned prior to the SEM and EDS measurements and thus may contain salt residues.

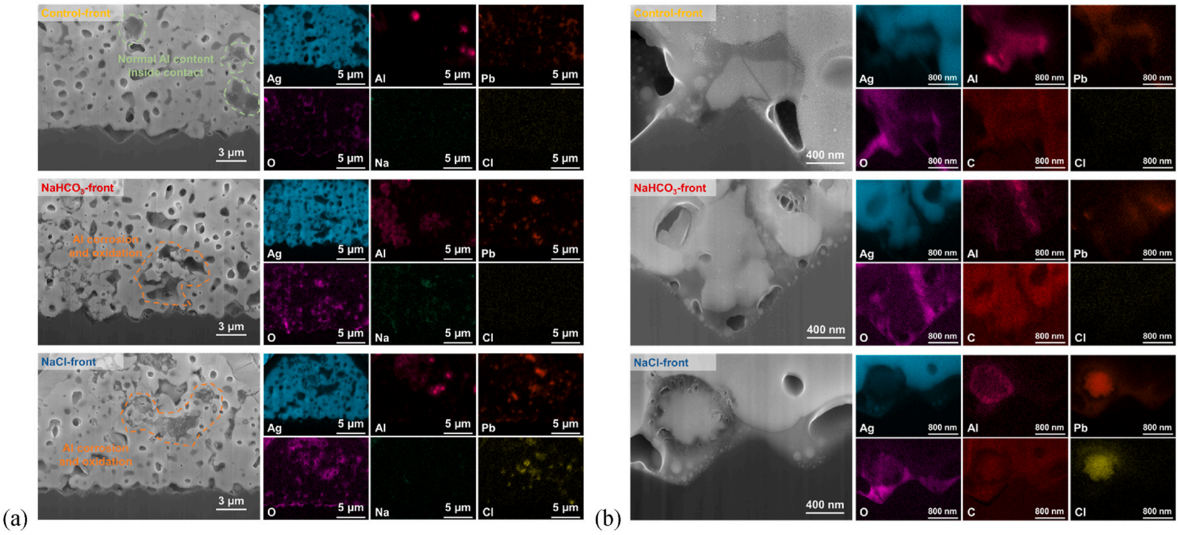

Fig. 10. (a) 5000 × and (b) 40,000 × Cross-section SEM images of front-side treated TOPCon samples after 100-h DH85 by cryo-FIB and corresponding EDS mappings of Ag, Al, Pb, O, Na and Cl.

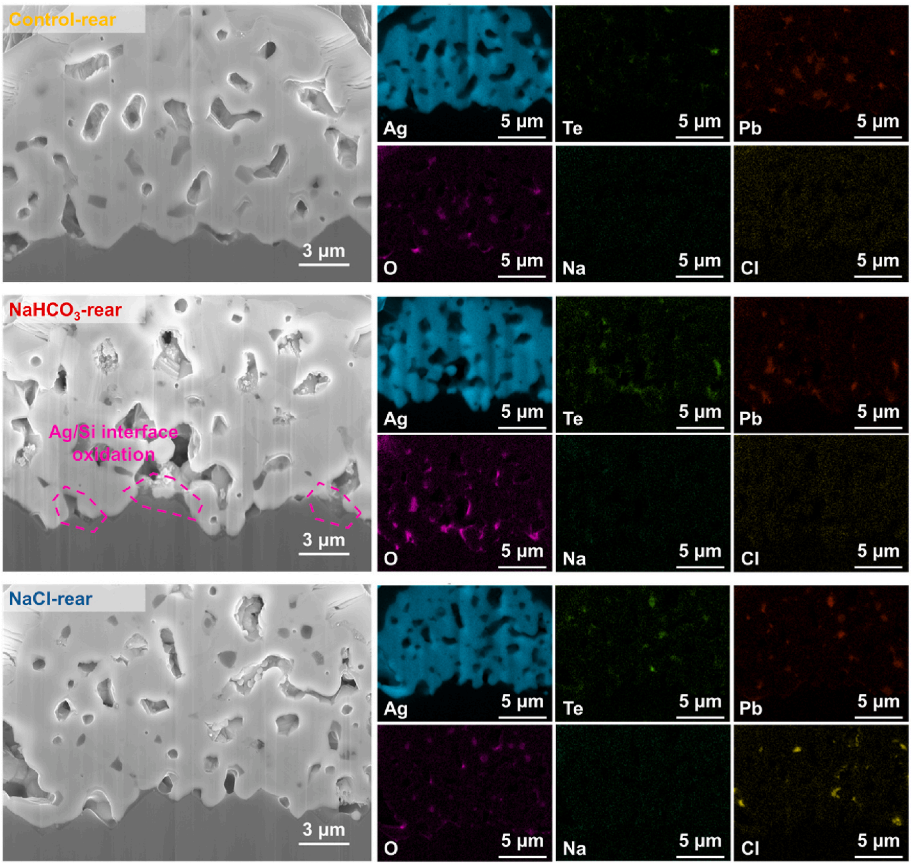

Fig. 11. Cross-section SEM images of rear-side treated TOPCon samples after 100-h DH85 by cryo-FIB and corresponding EDS mappings of Ag, Te, Pb, O, Na and Cl.

surfaces. This Ag/Al spike phenomenon has been extensively documented in the literature as contributing to the formation of ohmic contacts on boron-diffused emitters [45,52–54]. However, both $NaHCO_3$ and NaCl degraded the contact interfaces, with voids likely forming at the interface after DH85 testing. The distribution of Al at the interface was also affected during the degradation period. The Al-spike structures were no longer as pronounced as those displayed in the Control-front sample in Fig. 10 (b), indicating damage to the ohmic contact formed at the metal/Si interface. Furthermore, for the NaCl-front sample, Cl in proximity to Pb was observed at the interface, suggesting deterioration of the interface glass frit. As the interface glass frit degraded, the binding between the metal and Si weakened. Consequently, $NaHCO_3$ and NaCl caused varying degrees of resistance increase in the TOPCon solar cells.

As depicted in Fig. 11, the FIB-SEM images and corresponding EDS analysis provides insight into the rear-side contract failure mechanisms.

In Control-rear samples, the primary glass used were TeO_2 and PbO, with Ag being the sole conductive element detected, while Al was absent. This configuration is advantageous as Ag can readily form contact with poly-Si, exhibiting excellent electron conductivity and extraction in n-type TOPCon cells [55–58]. Similar to the Control-front sample, no traces of Na or Cl were observed in the Control-rear sample, as shown in Fig. 11. However, $NaHCO_3$-rear samples exhibited localised dark regions at the Ag and Si interface. Combined with EDS analysis, the interface between metal/Si was locally heavily oxidised, indicating reduced conductivity and potentially contributing to the observed increase in R_s. Particularly, the heightened O signals at the Si/Ag interface in $NaHCO_3$-rear samples underscore severe oxidation issues, surpassing typical glass frit and interface oxide sizes seen in the Control-rear sample. These findings confirm the deterioration at the Si/Ag contact interface. The contact edge oxidation was not observed in the $NaHCO_3$-front samples, which could be attributed to the SiO_yN_z layer on the front side. This layer may facilitate the formation of a more stable interface structure between the outer edge where the metal and silicon surfaces meet upon firing (Ag-O-Si), compared to the Ag-Si structure, thereby preventing issues observed on the rear side.

From Fig. 11, NaCl-rear samples maintained a similar non-oxidised Si/Ag interface to the Control-rear, suggesting a lack of contribution to rear-side contact failure, which contrasts sharply with front-side failures. It is noteworthy that Cl signals were present within the metal contacts of NaCl-rear samples; however, unlike the front, Cl was less dispersed and not overlapping with Pb, indicating a different reaction mechanism that did not elevate R_s in NaCl-rear samples. Considering the discrepancies in material reactivity and elemental traces between NaCl-front and NaCl-rear, this information suggests that Al-free Ag paste is unlikely to undergo evident redox reactions during DH85 testing. This observation is consistent with the findings reported in our previously published work [33]. Al could potentially emerge as a critical factor in the instability of front-side contacts, a discussion that will be further elaborated in subsequent sections.

3.4. *XPS analysis*

To enhance our comprehension of the failure mechanisms occurring at the contact surface, we performed XPS analysis, as illustrated in Fig. 12. The analysis centred on the essential metallic components found in both the front and rear contacts. With a focus on surface element analysis, probing to a depth of approximately 10 nm, the XPS examination unveiled intriguing findings. The Control-front and Control-rear samples displayed two distinct Ag peaks, positioned at approximately ~369 eV for $Ag3d_{5/2}$ and ~375 eV for $Ag3d_{3/2}$. These peaks are indicative of Ag in its metallic state (Ag^0) [59–61]. The Pb peaks were identified at around ~139 eV for $Pb4f_{7/2}$ and ~144 eV for $Pb4f_{5/2}$, aligning with the Pb^{2+} state and suggesting Pb-O bonding typical of PbO [62–64].

The analysis uncovered the appearance of additional Ag peaks across all front-side samples exposed to contaminants. These peaks showed a shift to lower binding energies, located at approximately ~367 eV for $Ag3d_{5/2}$ and ~373 eV for $Ag3d_{3/2}$, suggesting the presence of Ag ions (Ag^+) [60,65]. This shift could be related to the Ag oxidation and is also likely to contribute to the decrease in conductance of the front-side contacts. Additionally, new Pb peaks were observed in the contaminated samples, also exhibiting lower binding energies than those associated with Pb^{2+}, potentially indicative of Pb^0 [64,66]. This suggests a partial reduction reaction occurring within PbO. Combined with the SEM and EDS analysis shown in Figs. 9 (a) and 10 (a), this reaction might also occur at the metal/Si contact interface, potentially leading to failures in contact resistivity. The fingerprints of Pb degradation could also be discerned in Fig. 10 (b), offering further evidence of glass frit degradation.

Following exposure to Na-containing salts on the rear side, no notable changes were observed in the peak positions or intensities of Ag and Pb after 100 h of DH85 testing. Despite a discernible decline in R_s, the chemical states of Ag and Pb remained constant. Figs. 9 (b) and 11 indicate that the deterioration at the rear contacts, prompted by $NaHCO_3$, primarily manifested at the Ag/Si interface. While Fig. 11 illustrates Cl penetration, it is plausible that NaCl might not induce significant chemical interactions with the rear metal contacts or substantially modify the properties of the metal and PbO. Hence, the R_s values for NaCl-rear samples remained relatively steady under DH85 conditions. Given the noteworthy composition variance, it is conceivable that Al could exert a significant influence on the degradation of contacts.

3.5. *Possible reaction principles of metal contact degradation*

From previous SEM, EDS and XPS analysis, post 100-h DH85 testing, the Ag structure remained largely unchanged, retaining its dense

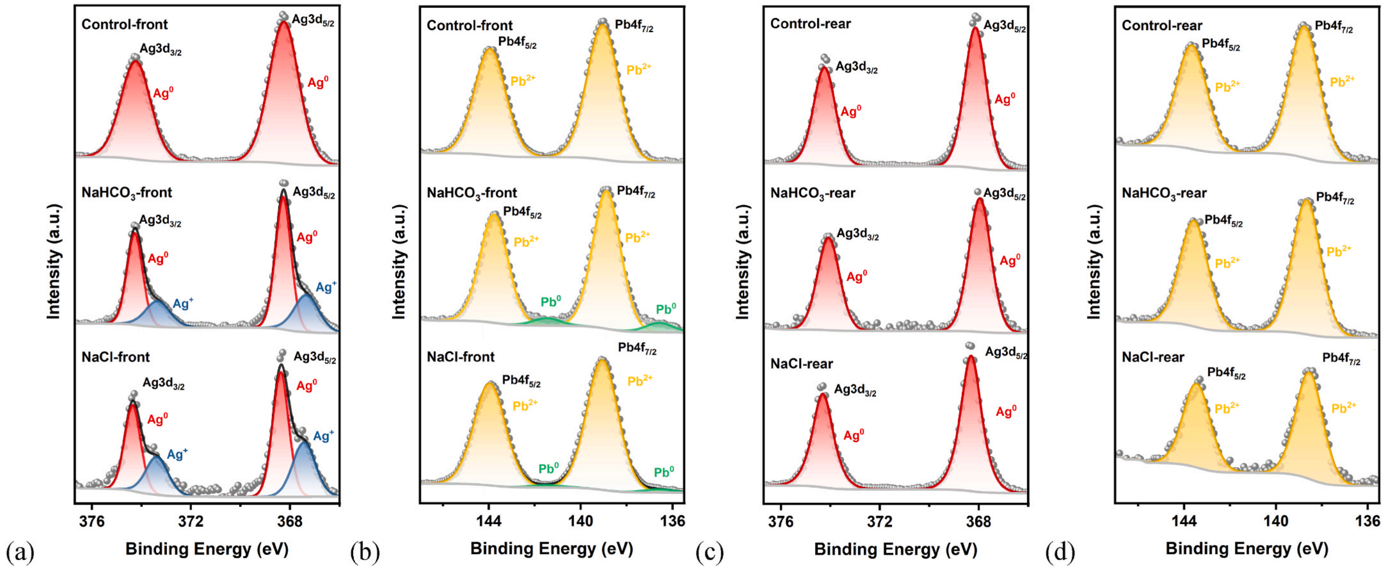

Fig. 12. XPS spectra for TOPCon solar cells of (a) Ag peaks and (b) Pb peaks of front-side contaminated groups, and (c) Ag peaks and (d) Pb peaks of rear-side contaminated groups underwent 100 h of DH85.

composition. Notably, induced contaminations were consistently detected around Al signal regions, accompanied by the presence of oxygen signals in proximity to these areas. The inherent electrochemical properties of Al and Ag, allowing for oxidation-reduction reactions [67,68], can develop internal electrochemical potentials. Also, metallic Pb was observed, likely due to a Pb reduction reaction. Under the influence of induced contamination, humidity, and elevated temperatures, these reactions may accelerate. Two sequential possible models have been proposed and outlined in Table 4 to describe these reactions.

All reactions involving contaminants during DH85 were based on ionisation, leading to an increased production of hydrogen ions (H^+) and hydroxide ions (OH^-). In this environment, metal Al loses electrons, converting into Al^{3+}, which then reacts with OH^- to form aluminium hydroxide [$Al(OH)_3$] [51,69–72]. As shown in Table 4, $NaHCO_3$ induces ionisation, producing Na^+ and HCO_3^-. HCO_3^- continues to generate OH- and carbonic acid (H_2CO_3), which decomposes into carbon dioxide (CO_2) and H_2O [73,74]. Limited H_2CO_3 may also react with PbO, releasing Pb^{2+} from the glass frit under DH85 conditions. OH^- further reacts with ionised Al ions to produce $Al(OH)_3$, which, unstable under damp-heat conditions, decomposes into chemically stable Al_2O_3 and H_2O. However, Al_2O_3, being an insulating material, contributes to gradual contact failure, evidenced by the observed increase in R_s. Additionally, limited Pb^{2+} may gather electrons from Al to form metallic Pb during DH85. Residual H^+ from ionisation initiates reactions with oxygen or other oxidising agents, extracting electrons from Al, completing the oxidation-reduction cycle.

The chlorine ion can form complexes with metal ions, thus accelerating metal corrosion [81–83]. NaCl, commonly used to evaluate alloy corrosion, triggers reactions in the front contact during DH85. Specifically, Al reacts according to Eqs. (2) and (3), while chlorination might occur in PbO as per Eq. (10) [84]. Previous research and literature emphasise the significant permeability of Cl^-, allowing it to penetrate $Al(OH)_3$ and Al_2O_3, leading to more ionisation of Al^{3+} during DH85 [24,77,85]. Consequently, most metallic Al in the contact converts into aluminium chloride or $Al_2O_3/Al(OH)_3$ [85,86]. Similarly to the $NaHCO_3$-front, some metallic Pb forms from the reduction reaction, as shown in Eq. (13). Observations in the NaCl-front show Pb signals mainly associated with Cl, along with voids containing Al, O, Na, and Cl signals. The combination of Pb and Cl affects the front contact, influencing electrical and mechanical properties, resulting in the delamination of metallisation and silicon-based surfaces, as previously noted [20]. Degradation of Al and PbO renders the TOPCon solar cells nearly inoperative within the test period in the NaCl-front group. However, treatment with $NaHCO_3$ leads to slower and less significant contact degradation. This difference primarily arises from the larger anion size and chemical activity of these salts due to their polyatomic combination structures, which hinder direct access to the Al surface. Additionally, the Al corrosion by-products of $NaHCO_3$, primarily $Al(OH)_3$ and Al_2O_3, could be likely to passivate the Al surface, resulting in a lower corrosion rate. Following the reaction, limited Na is detected in the NaCl-front contact, suggesting possible diffusion into deeper cell regions, exacerbating recombination issues.

The rear-side contacts experienced significant failure when treated with alkali salts like $NaHCO_3$. These salts, resulting from incomplete neutralisation of strong bases and weak acids, exhibit alkalinity in aqueous environments and release OH^- [87–89]. In Figs. 9 (b) and 11, SEM-EDS analysis consistently showed an accumulation of Na and O signals along the exposed regions of the Si-Ag boundary, indicating potential corrosion at the Ag/Si interface. In contrast to the front-side contacts, the rear side of the control group, coated with SiN_x:H, have a lower O concentration. Consequently, the rear-side metallisation experienced reduced oxygen intervention, which may have promoted the formation of an Ag/Si alloy at the interface rather than an Ag-O-Si structure. Under damp-heat conditions, $NaHCO_3$, for instance, as shown in Eqs. (4) and (5), could readily hydrolyse to produce OH^-. Ag/Si alloy might undergo corrosion in basic settings, following reactions depicted in Eqs. (15) and (16). Consequently, Si might exist partly as SiO_2, while some could combine with Na^+ in the form of acid radicals, such as SiO_3^{2-}, after DH85 testing [90,91]. The increased SiO_2 thickness could hinder Na accumulation on the surface, explaining the observed EDS element distributions.

$$Ag - Si_{(s)} + 4H_2O_{(aq)} \rightarrow Ag_{(s)} + Si(OH)_{4\,(aq)} + 2H_{2\,(g)} \qquad \text{(Eq. 15)}$$

$$Si(OH)_{4\,(aq)} + OH^- \rightarrow H_3SiO_4^- + H_2O_{(aq)} \qquad \text{(Eq. 16)}$$

This reaction influenced the oxide formation from $NaHCO_3$ between Si and Ag, resulting in larger oxide sizes compared to normal glass frit (Fig. 11). Consequently, carrier transportation faced greater impedance, elevating contact resistivity and impacting the cells' R_s. However, NaCl exhibited no discernible impact on the rear-side contact. Cl signals primarily resided in void regions, with limited observable overlap between Cl and Pb EDS mappings. Considering our prior theory on front contact failures, where Ag was the primary conductive component at the rear side without any other active metals in the contact under neutral conditions, there existed no driving force for Cl to combine with Pb.

Recently, the introduction of laser-assisted firing [such as laser-enhanced contact optimisation (LECO)] has enabled the application of Al-free Ag paste on the front side of TOPCon solar cells. This technique achieves excellent ohmic contact [33,92,93]. Our previous research demonstrated that Al-free front-side Ag contacts exhibit significantly better reliability compared to Ag/Al paste under NaCl-induced DH85 testing, highlighting the critical role of Al in front-side contact degradation [33].

4. Conclusion

This study explores the accelerated degradation of industrial TOPCon solar cells subjected to DH85 testing, focusing on the impact of two different Na-related salts, $NaHCO_3$ and NaCl, as contaminants. The study observes varying degradation levels after 100-h DH85 testing, particularly affecting the front and rear sides of the solar cells. Front-side

Table 4

Possible chemical reactions induced by $NaHCO_3$ and NaCl on the front metal contacts of TOPCon solar cells [51,71,74–80].

Possible chemical reactions by $NaHCO_3$	Possible chemical reactions by NaCl
$H_2O_{(aq)} \rightarrow H^+ + OH^-$ (Eq.1)	
$Al_{(s)} - 3e^- \rightarrow Al^{3+}$ (Eq. 2)	
$Al^{3+} + 3OH^- \rightarrow Al(OH)_{3\,(aq/s)}$ (Eq. 3)	
$NaHCO_{3\,(s)} \rightarrow Na^+ + HCO_3^-$ (Eq. 4)	$NaCl_{(s)} \rightarrow Na^+ + Cl^-$ (Eq. 8)
$HCO_3{}^- + H_2O_{(aq)} \rightarrow H_2CO_{3\,(aq)} + OH^-$ (Eq. 5)	$Cl^- + H_2O_{(aq)} \rightarrow HCl_{(aq)} + OH^-$ (Eq. 9)
$H_2CO_{3\,(aq)} + PbO_{(s)} \rightarrow Pb^{2+} + CO_3^{2-} + H_2O_{(aq)}$ (Eq. 6)	$2HCl_{(aq)} + PbO_{(s)} \rightarrow Pb^{2+} + 2Cl^- + H_2O_{(aq)}$ (Eq. 10)
$Al^{3+} + 3HCO_3{}^- \rightarrow Al(OH)_{3\,(aq/s)} + 3CO_{2\,(g)}$ (Eq. 7)	$Al^{3+} + 3Cl^- \rightarrow AlCl_{3(aq/s)}$ (Eq. 11)
$2Al(OH)_{3\,(aq/s)} \rightarrow Al_2O_{3\,(s)} + 3H_2O_{(aq)}$ (Eq. 12)	
$Pb^{2+} + 2e^- \rightarrow Pb_{(s)}$ (Eq. 13)	
$4H^+ + 4e^- + O_{2\,(g)} \rightarrow 2H_2O_{(aq)}$ (Eq. 14)	

degradation primarily involves contact-related issues, with NaCl demonstrating the most severe effects, resulting in a relative *PCE* reduction of approximately 92 % after 100-h DH85 testing. This reduction is mainly attributed to increased R_s complemented by a decrease in J_{sc} resulting from inadequate current extraction. Rear-side contamination led to an increase in recombination, possibly due to Na infiltration through degraded ARC layers, resulting in drops in V_{oc} and J_{sc}. Furthermore, $NaHCO_3$ treatment could increase local R_s values with approximately 16.0 % relative *PCE* drop. However, NaCl did not notably impact rear R_s.

This manuscript mainly focuses on metal contact failures and proposes several degradation models. These suggest that front-side contact failures primarily stem from oxidation-reduction reactions between Al, Ag and PbO within the metal contacts, particularly highlighting the susceptibility of the Ag/Al paste to long-term stability risks, especially when exposed to ion-level contaminants. These models elucidate differences in front contact degradation mechanisms among NaCl and $NaHCO_3$, potentially extending their applicability to other ion combinations. Regarding the rear side, alkaline conditions may have contributed to rear-side contact deterioration involving $NaHCO_3$.

In summary, this study unveils that TOPCon contact degradation mechanisms are significantly influenced by the combination of ions and paste compositions. The findings offer crucial insights into the degradation patterns and underlying factors affecting the metal contacts of TOPCon solar cells, potentially aiding in the evaluation of module-level reliability. The research advocates for expanded accelerated testing methods and highlights opportunities for optimising processes to bolster the long-term reliability of TOPCon cells or modules in practical applications.

CRediT authorship contribution statement

Xinyuan Wu: Writing – review & editing, Writing – original draft, Visualization, Software, Methodology, Investigation, Formal analysis, Data curation, Conceptualization. **Chandany Sen:** Writing – review & editing, Methodology, Investigation. **Xutao Wang:** Investigation, Formal analysis, Data curation, Conceptualization. **Yuhao Cheng:** Investigation, Data curation. **Ruirui Lv:** Validation, Resources, Investigation, Data curation. **Hao Song:** Resources, Investigation. **Yuanjie Yu:** Project administration, Investigation. **Baochen Liao:** Writing – review & editing, Methodology, Investigation. **Sheng Ma:** Investigation, Formal analysis. **Muhammad Umair Khan:** Methodology, Investigation. **Alison Ciesla:** Writing – review & editing, Supervision, Investigation. **Bram Hoex:** Writing – review & editing, Visualization, Supervision, Project administration, Investigation, Funding acquisition.

Declaration of competing interest

The authors declare the following financial interests/personal relationships which may be considered as potential competing interests:

Bram Hoex reports financial support was provided by Australian Renewable Energy Agency. Bram Hoex reports financial support was provided by University of New South Wales. If there are other authors, they declare that they have no known competing financial interests or personal relationships that could have appeared to influence the work reported in this paper.

Data availability

Data will be made available on request.

Acknowledgements

This work received support from theAustralian Government through the Australian Renewable Energy Agency (ARENA 1–060 Extension project) and the Australian Centre for Advanced Photovoltaics (ACAP). The authors appreciate the support provided by the Australian Government's Trailblazer for Recycling & Clean Energy program, led by UNSW & the University of Newcastle. However, the Australian Government does not accept responsibility for the views, information, or advice expressed in this research. The authors would like to acknowledge the Electron Microscope Unit at The University of New South Wales (UNSW), specifically Dr Charlie Kong, Dr Yin Yao and Dr Karen Privat for their scientific and technical assistance and access to the facilities of the Australian Microscopy & Microanalysis Research Facility. The authors acknowledge the surface analysis laboratory, Solid State & Elemental Analysis Unit (SSEAU), Mark Wainwright Analytical Centre (MWAC), and UNSW for the support of XPS analysis. The authors also express their gratitude for the support provided by the entire team at the Solar Industrial Research Facility (SIRF) at UNSW.

References

[1] F. Feldmann, M. Bivour, C. Reichel, M. Hermle, S.W. Glunz, A passivated rear contact for high-efficiency n-type silicon solar cells enabling high Vocs and FF> 82%, in: 28th European PV Solar Energy Conference and Exhibition, 2013.

[2] F. Feldmann, M. Bivour, C. Reichel, M. Hermle, S.W. Glunz, Passivated rear contacts for high-efficiency n-type Si solar cells providing high interface passivation quality and excellent transport characteristics, Sol. Energy Mater. Sol. Cell. 120 (2014) 270–274.

[3] A. Richter, et al., Design rules for high-efficiency both-sides-contacted silicon solar cells with balanced charge carrier transport and recombination losses, Nat. Energy 6 (4) (2021-04-01 2021) 429–438, https://doi.org/10.1038/s41560-021-00805-w.

[4] F. Feldmann, et al., Large area TOPcon cells realized by a PECVD tube process, in: Proc. 36th Eur. Photovolt. Sol. Energy Conf. Exhib., 2019, pp. 304–308.

[5] S. Duttagupta, N. Nandakumar, P. Padhamnath, J.K. Buatis, R. Stangl, A.G. Aberle, monoPoly™ cells: large-area crystalline silicon solar cells with fire-through screen printed contact to doped polysilicon surfaces, Sol. Energy Mater. Sol. Cell. 187 (2018-12-01 2018) 76–81, https://doi.org/10.1016/j.solmat.2018.05.059.

[6] A. Richter, et al., Tunnel oxide passivating electron contacts as full-area rear emitter of high-efficiency p-type silicon solar cells, Prog. Photovoltaics Res. Appl. 26 (8) (2018) 579–586.

[7] A. Richter, J. Benick, F. Feldmann, A. Fell, M. Hermle, S.W. Glunz, n-Type Si solar cells with passivating electron contact: identifying sources for efficiency limitations by wafer thickness and resistivity variation, Sol. Energy Mater. Sol. Cell. 173 (2017) 96–105.

[8] B. Liao, et al., Atomic scale controlled tunnel oxide enabled by a novel industrial tube-based PEALD technology with demonstrated commercial TOPCon cell efficiencies > 24%, Prog. Photovoltaics Res. Appl. 31 (3) (2023-03-01 2023) 220–229, https://doi.org/10.1002/pip.3627.

[9] B. Liao, et al., Tube type plasma enhanced atomic layer deposition of aluminum oxide: enabling record lab performance for the industry with demonstrated cell efficiencies >24%, Prog. Photovoltaics Res. Appl. 31 (1) (2023-01-01 2023) 52–61, https://doi.org/10.1002/pip.3607.

[10] B. Liao, J. Ge, X. Wu, Q. Wang, R.J. Yeo, Z. Du, Unlocking the potential of boronsilicate glass passivation for industrial tunnel oxide passivated contact solar cells, Prog. Photovoltaics Res. Appl. 30 (3) (2022) 310–317.

[11] W. Chen, et al., N-type polysilicon passivating contacts using ultra-thin PECVD silicon oxynitrides as the interfacial layer, Sol. Energy Mater. Sol. Cell. 232 (2021-10-01 2021) 111356, https://doi.org/10.1016/j.solmat.2021.111356.

[12] D. Chen, et al., 24.58% total area efficiency of screen-printed, large area industrial silicon solar cells with the tunnel oxide passivated contacts (i-TOPCon) design, Sol. Energy Mater. Sol. Cell. 206 (2020) 110258.

[13] C. Liu, et al., Industrial TOPCon solar cells on n-type quasi-mono Si wafers with efficiencies above 23, Sol. Energy Mater. Sol. Cell. 215 (2020-09-01 2020) 110690, https://doi.org/10.1016/j.solmat.2020.110690.

[14] M.A. Green, et al., Solar cell efficiency tables (Version 64), Prog. Photovoltaics Res. Appl. 32 (7) (2024-07-01 2024) 425–441, https://doi.org/10.1002/pip.3831.

[15] M. Fischer, M. Woodhouse, P. Baliozian, J. Trube, International Technology Roadmap for Photovoltaic (ITRPV) 2022 Results, VDMA, 2023.

[16] S. Chunduri, Monthly TaiyangNews update on commercially available high efficiency solar modules. https://taiyangnews.info/top-solar-modules-listing-june-2024/. (Accessed 14 July 2024).

[17] I.M. Peters, J. Hauch, C. Brabec, P. Sinha, The value of stability in photovoltaics, Joule 5 (12) (2021/12/15/2021) 3137–3153, https://doi.org/10.1016/j.joule.2021.10.019.

[18] P.M. Sommeling, J. Liu, J.M. Kroon, Corrosion effects in bifacial crystalline silicon PV modules; interactions between metallization and encapsulation, Sol. Energy Mater. Sol. Cell. 256 (2023/07/01/2023) 112321, https://doi.org/10.1016/j.solmat.2023.112321.

[19] N. Iqbal, et al., Impact of acetic acid exposure on metal contact degradation of different crystalline silicon solar cell technologies, Sol. Energy Mater. Sol. Cell. 250 (2023/01/15/2023) 112089, https://doi.org/10.1016/j.solmat.2022.112089.

[20] C. Sen, et al., Accelerated damp-heat testing at the cell-level of bifacial silicon HJT, PERC and TOPCon solar cells using sodium chloride, Sol. Energy Mater. Sol. Cell. 262 (2023/10/15/2023) 112554, https://doi.org/10.1016/j.solmat.2023.112554.

[21] O.K. Segbefia, A.G. Imenes, T.O. Sætre, Moisture ingress in photovoltaic modules: a review, Sol. Energy 224 (2021/08/01/2021) 889–906, https://doi.org/10.1016/j.solener.2021.06.055.

[22] M.D. Kempe, Modeling of rates of moisture ingress into photovoltaic modules, Sol. Energy Mater. Sol. Cell. 90 (16) (2006/10/16/2006) 2720–2738, https://doi.org/10.1016/j.solmat.2006.04.002.

[23] O.K. Segbefia, N. Akhtar, T.O. Sætre, Moisture induced degradation in field-aged multicrystalline silicon photovoltaic modules, Sol. Energy Mater. Sol. Cell. 258 (2023/08/15/2023) 112407, https://doi.org/10.1016/j.solmat.2023.112407.

[24] X. Wu, et al., Addressing sodium ion-related degradation in SHJ cells by the application of nano-scale barrier layers, Sol. Energy Mater. Sol. Cell. 264 (2024/01/01/2024) 112604, https://doi.org/10.1016/j.solmat.2023.112604.

[25] X. Li, et al., Potential-free sodium-induced degradation of silicon heterojunction solar cells, Prog. Photovoltaics Res. Appl. (2023), https://doi.org/10.1002/pip.3698.

[26] X. Li, et al., Highly crystallized tungsten doped indium oxide film stabilizes silicon heterojunction solar cells in sodium environment, Sol. Energy Mater. Sol. Cell. 233 (2021/12/01/2021) 111387, https://doi.org/10.1016/j.solmat.2021.111387.

[27] M.U. Khan, et al., Supercharging cell-level potential-induced degradation (PID) testing using a salt-enriched hybrid polymer layer, Sol. Energy Mater. Sol. Cell. 260 (2023/09/15/2023) 112479, https://doi.org/10.1016/j.solmat.2023.112479.

[28] W. Luo, et al., Potential-induced degradation in photovoltaic modules: a critical review, Energy Environ. Sci. 10 (1) (2017-01-01 2017) 43–68, https://doi.org/10.1039/c6ee02271e.

[29] D. Adachi, T. Terashita, T. Uto, J.L. Hernández, K. Yamamoto, Effects of SiOx barrier layer prepared by plasma-enhanced chemical vapor deposition on improvement of long-term reliability and production cost for Cu-plated amorphous Si/crystalline Si heterojunction solar cells, Sol. Energy Mater. Sol. Cell. 163 (2017/04/01/2017) 204–209, https://doi.org/10.1016/j.solmat.2016.12.029.

[30] Z. Sharp, D. Draper, The chlorine abundance of Earth: implications for a habitable planet, Earth Planet Sci. Lett. 369 (2013) 71–77.

[31] T.E. Graedel, W. Keene, The budget and cycle of Earth's natural chlorine, Pure Appl. Chem. 68 (9) (1996) 1689–1697.

[32] A.J. Magenheim, A.J. Spivack, P.J. Michael, J.M. Gieskes, Chlorine stable isotope composition of the oceanic crust: implications for Earth's distribution of chlorine, Earth Planet Sci. Lett. 131 (3–4) (1995) 427–432.

[33] X. Wu, et al., Enhancing the reliability of TOPCon technology by laser-enhanced contact firing, Sol. Energy Mater. Sol. Cell. 271 (2024/07/01/2024) 112846, https://doi.org/10.1016/j.solmat.2024.112846.

[34] C. Peike, et al., Origin of damp-heat induced cell degradation, Sol. Energy Mater. Sol. Cell. 116 (2013) 49–54.

[35] I. Duerr, J. Bierbaum, J. Metzger, J. Richter, D. Philipp, Silver grid finger corrosion on snail track affected PV modules–investigation on degradation products and mechanisms, Energy Proc. 98 (2016) 74–85.

[36] N. Kyranaki, et al., Damp-heat induced degradation in photovoltaic modules manufactured with passivated emitter and rear contact solar cells, Prog. Photovoltaics Res. Appl. 30 (9) (2022-09-01 2022) 1061–1071, https://doi.org/10.1002/pip.3556.

[37] A.M. Jeffries, T. Nietzold, L.T. Schelhas, M.I. Bertoni, Corrosion of novel reactive silver ink and commercial silver-based metallizations in diluted acetic acid, Sol. Energy Mater. Sol. Cell. 223 (2021/05/01/2021) 110900, https://doi.org/10.1016/j.solmat.2020.110900.

[38] D.N.R. Payne, C. Vargas, Z. Hameiri, S.R. Wenham, D.M. Bagnall, An advanced software suite for the processing and analysis of silicon luminescence images, Comput. Phys. Commun. 215 (2017/06/01/2017) 223–234, https://doi.org/10.1016/j.cpc.2017.02.012.

[39] H. Kampwerth, T. Trupke, J. Weber, Y. Augarten, Advanced luminescence based effective series resistance imaging of silicon solar cells, Appl. Phys. Lett. 93 (20) (2008) 202102.

[40] J. Wong, Griddler: intelligent computer aided design of complex solar cell metallization patterns, in: 2013 IEEE 39th Photovoltaic Specialists Conference (PVSC), IEEE, 2013, pp. 933–938.

[41] W. Li, et al., Effects of silver nanoparticles on the firing behavior of silver paste on crystalline silicon solar cells, Colloids Surf. A Physicochem. Eng. Asp. 466 (2015) 132–137.

[42] D. Chen, L. Zhao, H. Diao, W. Zhang, G. Wang, W. Wang, Low-temperature sintering properties of the screen-printed silver paste for a-Si: H/c-Si heterojunction solar cells, J. Mater. Sci. Mater. Electron. 25 (2014) 2657–2664.

[43] M.M. Hilali, et al., Effect of Ag particle size in thick-film Ag paste on the electrical and physical properties of screen printed contacts and silicon solar cells, J. Electrochem. Soc. 153 (1) (2005) A5.

[44] J.D. Fields, et al., The formation mechanism for printed silver-contacts for silicon solar cells, Nat. Commun. 7 (1) (2016/04/01 2016) 11143, https://doi.org/10.1038/ncomms11143.

[45] S. Fritz, M. König, S. Riegel, A. Herguth, M. Hörteis, G. Hahn, Formation of Ag/Al screen-printing contacts on B emitters, IEEE J. Photovoltaics 5 (1) (2014) 145–151.

[46] F. Kiefer, J. Krügener, F. Heinemeyer, H.J. Osten, R. Brendel, R. Peibst, Structural investigation of printed Ag/Al contacts on silicon and numerical modeling of their contact recombination, IEEE J. Photovoltaics 6 (5) (2016) 1175–1182.

[47] L. Liang, Z. Li, L.K. Cheng, N. Takeda, R. Young, A. Carroll, Current conduction mechanism of front-side contact of N-type crystalline Si solar cells with Ag/Al pastes, IEEE J. Photovoltaics 4 (2) (2013) 549–553.

[48] G. Aullón, D. Bellamy, A.G. Orpen, L. Brammer, E.A. Bruton, Metal-bound chlorine often accepts hydrogen bonds, Chem. Commun. (6) (1998) 653–654.

[49] Y.-N. Chang, F.-I. Wei, High-temperature chlorine corrosion of metals and alloys: a review, J. Mater. Sci. 26 (1991) 3693–3698.

[50] M. Edwards, A. Dudi, Role of chlorine and chloramine in corrosion of lead bearing plumbing materials, J. Am. Water Works Assoc. 96 (10) (2004) 69–81.

[51] T. Graedel, Corrosion mechanisms for aluminum exposed to the atmosphere, J. Electrochem. Soc. 136 (4) (1989) 204C.

[52] G. Xing, W. Chen, Y. Liu, X. Du, Al-induced variation to Ag crystal orientation of Ag–Al pastes during metallization, Sol. Energy Mater. Sol. Cell. 270 (2024/06/15/2024) 112814, https://doi.org/10.1016/j.solmat.2024.112814.

[53] S. Fritz, S. Riegel, A. Hammud, H. Deniz, G. Hahn, Crystalline nature of metal spikes and silicon inclusions in Ag/Al screen-printing metallization, IEEE J. Photovoltaics 6 (1) (2015) 79–85.

[54] E. Lohmüller, S. Werner, R. Hoenig, J. Greulich, F. Clement, Impact of boron doping profiles on the specific contact resistance of screen printed Ag–Al contacts on silicon, Sol. Energy Mater. Sol. Cell. 142 (2015) 2–11.

[55] Y. Zeng, et al., Theoretical exploration towards high-efficiency tunnel oxide passivated carrier-selective contacts (TOPCon) solar cells, Sol. Energy 155 (2017) 654–660.

[56] F.-J. Ma, et al., Advanced modeling of the effective minority carrier lifetime of passivated crystalline silicon wafers, J. Appl. Phys. 112 (5) (2012) 054508.

[57] F. Feldmann, C. Reichel, R. Müller, M. Hermle, The application of poly-Si/SiOx contacts as passivated top/rear contacts in Si solar cells, Sol. Energy Mater. Sol. Cell. 159 (2017-01-01 2017) 265–271, https://doi.org/10.1016/j.solmat.2016.09.015.

[58] J. Schmidt, R. Peibst, R. Brendel, Surface passivation of crystalline silicon solar cells: present and future, Sol. Energy Mater. Sol. Cell. 187 (2018-12-01 2018) 39–54, https://doi.org/10.1016/j.solmat.2018.06.047.

[59] A. Zielińska, et al., Silver-doped TiO2 prepared by microemulsion method: surface properties, bio-and photoactivity, Separ. Purif. Technol. 72 (3) (2010) 309–318.

[60] A.B. de Paiva, et al., The negative photoconductivity of Ag/AgO grown by spray-pyrolysis, Surfaces 5 (1) (2022) 209–217.

[61] A. Al-Sarraj, K.M. Saoud, A. Elmel, S. Mansour, Y. Haik, Optoelectronic properties of highly porous silver oxide thin film, SN Appl. Sci. 3 (1) (2021-01-01 2021), https://doi.org/10.1007/s42452-020-04091-1.

[62] D. Xu, X. Tan, C. Chen, X. Wang, Removal of Pb (II) from aqueous solution by oxidized multiwalled carbon nanotubes, J. Hazard Mater. 154 (1–3) (2008) 407–416.

[63] H. Cai, et al., Reduction temperature-dependent nanoscale morphological transformation and electrical conductivity of silicate glass microchannel plate, Materials 12 (7) (2019) 1183.

[64] Y. Wang, et al., XPS study on changes of lead on the channel surface of microchannel plate reduced by hydrogen, in: IOP Conference Series: Materials Science and Engineering, vol. 490, IOP Publishing, 2019 022067, 2.

[65] A.K. Mohamedkhair, Q. Drmosh, Z.H. Yamani, Silver nanoparticle-decorated tin oxide thin films: synthesis, characterization, and hydrogen gas sensing, Frontiers in materials 6 (2019) 188.

[66] H. Abdel-Samad, P.R. Watson, An XPS study of the adsorption of lead on goethite (α-FeOOH), Appl. Surf. Sci. 136 (1–2) (1998) 46–54.

[67] D.E. Carter, Oxidation-reduction reactions of metal ions, Environ. Health Perspect. 103 (suppl 1) (1995) 17–19.

[68] V. Brabie, A study on the mechanism of reaction between refractory materials and aluminium deoxidised molten steel, Steel Res. 68 (2) (1997) 54–60.

[69] K. Nişancioğlu, H. Holtan, Cathodic polarization of aluminium in acetate-buffered chloride media, Electrochim. Acta 24 (12) (1979) 1229–1235.

[70] N. Giskeødegård, O. Blajiev, A. Hubin, H. Terryn, O. Hunderi, K. Nisancioglu, Properties of oxide formed on aluminium in aqueous acetate buffer, Mater. Sci. Forum 519–521 (2006-07-01 2006) 717–722. https://doi.org/10.4028/www.scientific.net/msf.519-521.717.

[71] R.B. Spacht, The corrosion resistance of aluminum and its alloys, J. Chem. Educ. 23 (5) (1946) 253.

[72] A.I. Onuchukwu, Corrosion inhibition of aluminum in alkaline medium. I: influence of hard bases, Mater. Chem. Phys. 20 (4–5) (1988) 323–332.

[73] F. Zheng, et al., Corrosion characteristics of aluminum in sodium bicarbonate aqueous solution at 50 C, Int. J. Electrochem. Sci. 14 (8) (2019) 7303–7316.

[74] D.B. Wellner, S.J. Couperthwaite, G.J. Millar, Influence of operating parameters during electrocoagulation of sodium chloride and sodium bicarbonate solutions using aluminium electrodes, J. Water Proc. Eng. 22 (2018) 13–26.

[75] Q. Zhang, Z. Zhang, On the electrochemical dealloying of Al-based alloys in a NaCl aqueous solution, Phys. Chem. Chem. Phys. 12 (7) (2010-01-01 2010) 1453–1472, https://doi.org/10.1039/b919313h.

[76] S.-W. Fu, C.C. Lee, A corrosion study of Ag–Al intermetallic compounds in chlorine-containing epoxy molding compounds, J. Mater. Sci. Mater. Electron. 28 (20) (2017-10-01 2017) 15739–15747, https://doi.org/10.1007/s10854-017-7467-4.

[77] L.F. Gomes, C.L. Kugelmeier, A. Garcia, C.A. Della Rovere, J.E. Spinelli, Influences of alloying elements and dendritic spacing on the corrosion behavior of Al–Si–Ag alloys, J. Mater. Res. Technol. 15 (2021/11/01/2021) 5880–5893, https://doi.org/10.1016/j.jmrt.2021.11.043.

[78] M. Fleischmann, M. Liler, The anodic oxidation of solutions of plumbous salts. Part 1.—the kinetics of deposition of α-lead dioxide from acetate solutions, Trans. Faraday Soc. 54 (1958) 1370–1381.

[79] X. Sun, et al., Lead acetate trihydrate precursor route to synthesize novel ultrafine lead oxide from spent lead acid battery pastes, J. Power Sources 269 (2014) 565–576.

[80] L. Zheng, et al., Improvement of Al2O3 films on graphene grown by atomic layer deposition with pre-H2O treatment, ACS Appl. Mater. Interfaces 6 (10) (2014-05-28 2014) 7014–7019, https://doi.org/10.1021/am501690g.

[81] D.W. Buzza, R.C. Alkire, Growth of corrosion pits on pure aluminum in 1M NaCl, J. Electrochem. Soc. 142 (4) (1995) 1104.

[82] M. Jingling, W. Jiuba, L. Gengxin, X. Chunhua, The corrosion behaviour of Al–Zn–In–Mg–Ti alloy in NaCl solution, Corrosion Sci. 52 (2) (2010) 534–539.

[83] M. Trueba, S.P. Trasatti, Study of Al alloy corrosion in neutral NaCl by the pitting scan technique, Mater. Chem. Phys. 121 (3) (2010) 523–533.

[84] X. Wang, et al., High-temperature chlorination of PbO and CdO induced by interaction with NaCl and Si/Al matrix, RSC Adv. 8 (60) (2018) 34449–34458.

[85] R. Grilli, M.A. Baker, J.E. Castle, B. Dunn, J.F. Watts, Localized corrosion of a 2219 aluminium alloy exposed to a 3.5% NaCl solution, Corrosion Sci. 52 (9) (2010/09/01/2010) 2855–2866, https://doi.org/10.1016/j.corsci.2010.04.035.

[86] O. Seri, The effect of NaCl concentration on the corrosion behavior of aluminum containing iron, Corrosion Sci. 36 (10) (1994/10/01/1994) 1789–1803, https://doi.org/10.1016/0010-938X(94)90132-5.

[87] M. Herrmann, Corrosion of silicon nitride materials in aqueous solutions, J. Am. Ceram. Soc. 96 (10) (2013-10-01 2013) 3009–3022, https://doi.org/10.1111/jace.12509.

[88] L. Qiu, D.A. Guzonas, J. Qian, Corrosion of silicon nitride in high temperature alkaline solutions, J. Nucl. Mater. 476 (2016/08/01/2016) 293–301, https://doi.org/10.1016/j.jnucmat.2016.04.056.

[89] M. Herrmann, J. Schilm, G. Michael, J. Meinhardt, R. Flegler, Corrosion of silicon nitride materials in acidic and basic solutions and under hydrothermal conditions, J. Eur. Ceram. Soc. 23 (4) (2003) 585–594.

[90] V.E. Saouma, R.A. Martin, M.A. Hariri-Ardebili, T. Katayama, A mathematical model for the kinetics of the alkali–silica chemical reaction, Cement Concr. Res. 68 (2015/02/01/2015) 184–195, https://doi.org/10.1016/j.cemconres.2014.10.021.

[91] T. Ichikawa, M. Miura, Modified model of alkali-silica reaction, Cement Concr. Res. 37 (9) (2007/09/01/2007) 1291–1297, https://doi.org/10.1016/j.cemconres.2007.06.008.

[92] T. Fellmeth, et al., Laser enhanced contact optimization on iTOPCon solar cells, Prog. Photovoltaics Res. Appl. 30 (12) (2022) 1393–1399.

[93] Y. Fan, et al., Investigation of the Ag–Si contact characteristics of boron emitters for n-tunnel oxide-passivated contact solar cells metallized by laser-assisted current injection treatment, Sol. RRL n/a (n/a) (2024/06/05 2024) 2400268, https://doi.org/10.1002/solr.202400268.